# Beam Modulation and Bump-on-tail Effects On Alfvén Eigenmode Stability in DIII-D

**M.A. Van Zeeland[1], L. Bardoczi[1], J. Gonzalez-Martin[2], W.W. Heidbrink[3], M. Podesta[4], M. Austin[5], C.S Collins[1], X.D. Du[1], V.N. Duarte[4], M. Garcia-Munoz[2], S. Munaretto[1], K. Thome[1], Y. Todo[6], X. Wang[7]**

[1]General Atomics, P.O. Box 85608 San Diego, California 92186-5608, USA
[2]Department of Atomic, Molecular and Nuclear Physics, Universidad de Sevilla, Avenida de la Reina Mercedes s/n, 41012 Seville, Spain
[3]University of California at Irvine, Irvine, CA 92697, USA
[4]Princeton Plasma Physics Laboratory, PO Box 451, Princeton, NJ USA
[5]University of Texas at Austin, Austin, Texas 78712, USA
[6]National Institute for Fusion Science, Toki, Gifu 509-5292, Japan
[7]Max-Planck-Institut fur Plasmaphysik, Boltzmannstr. 2, 85748 Garching, Germany

**Abstract.** Beam modulation effects on Alfvén Eigenmode stability have been investigated in a recent DIII-D experiment and show that variations in neutral beam modulation period can have an impact on the beam driven Alfvén eigenmode spectrum and resultant fast ion transport despite similar time-averaged input power. The experiment was carried out during the current ramp phase of L-mode discharges heated with sub-Alfvénic 50-80 kV deuterium neutral beams that drive a variety of Alfvén eigenmodes unstable. The modulation period of two interleaved beams with different tangency radii was varied from shot to shot in order to modify the relative time dependent mix of the beam pitch angle distribution as well as the persistence of a bump-on-tail feature near the injection energy (a feature confirmed by Imaging Neutral Particle Analyzer (INPA) measurements). As the beam modulation period is varied from 7 ms to 30 ms on/off (typical full energy slowing down time of $\tau_{slow} \approx 50$ ms at mid-radius), toroidicity-induced Alfvén eigenmodes (TAEs) located in the outer periphery of the plasma become intermittent and coincident with the more tangential beam. Core mode activity changes from reversed shear Alfvén eigenmodes (RSAEs) to a mix of RSAE and beta-induced Alfvén eigenmodes (BAE). Discharges with 30 ms on/off period do not have a persistent bump-on-tail feature, have the lowest average mode amplitude and least fast ion transport. Detailed analysis of an individual TAE using TRANSP kick modeling (Monte Carlo evolution of the distribution function with probabilistic "kicks" by the AEs) and the resistive MHD code with kinetic fast ions, MEGA, find no strong role of energy gradient drive due to bump-on-tail features. Instead, the observed TAE modulation with interleaved beams is likely a pitch angle dependent result combined with slowing down of the tangential beam between pulses. For the conditions investigated, bump-on-tail contributions to TAE drive were found to be 5% or less of the total drive at any given time.

# 1. INTRODUCTION

High energy neutral beam modulation is a common technique used in fusion experiments for regulation of injected power and various diagnostic applications; however, the modulation period or duty cycle is often chosen arbitrarily or to accommodate hardware constraints without regard for the physics implications. When one beam is temporarily turned off or replaced by an unlike beam (different geometry or injection voltage), a bump-on-tail like distribution in velocity space is transiently created that can provide free energy for instability drive(1; 2). The persistence of the bump-on-tail feature depends on, among other things, the modulation period. Continuous modulation which is fast compared to the slowing down time creates a more persistent velocity space inversion while slow modulation transiently creates a bump-on-tail associated with each beam pulse before filling in. For heating scenarios where different modulated beams are interleaved, the time-dependent mix also depends heavily on the modulation period. Example TRANSP(3) calculated beam ion distribution functions for three typical DIII-D modulation scenarios are given in Figure 1, where that for a continuous beam, a beam modulated on/off every 10 ms, and two different interleaved beams both modulated 10 ms on/off but out of phase, are shown in Figures 1a, 1b and 1c respectively. Bump-on-tail velocity space features like those in Figure 1 are consistently observed on the new Imaging Neutral Particle Analyzer (INPA)(4; 5; 6) diagnostic on DIII-D, and, in fact, those measurements provided much of the impetus for this study.

As has been shown in many experiments (7; 8; 9; 10; 11; 12; 13; 5; 14; 15; 16), Alfvén eigenmodes (AEs) can severely limit performance as well as potentially damage device integrity(7; 17). A key component to predicting and understanding AE stability, and potentially controlling the modes, is having accurate predictions for all the important drive and damping mechanisms. While AEs in DIII-D, and other beam-heated plasmas, are typically thought to be driven predominantly by radial gradients of the fast ion pressure and damped by (among other effect such as radiative and collisional damping) the negative energy gradient found in beam ion slowing down distributions(18; 19; 20), this intuition is built upon an assumption of having a steady isotropic slowing down distribution or even a Maxwellian. The bump-on-tail
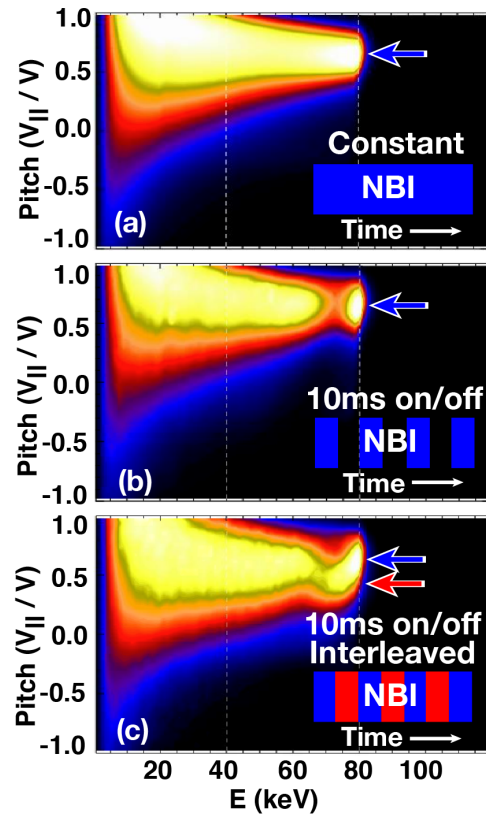


**Figure 1.** Example volume-averaged TRANSP distribution functions for: (a) Steady tangential NBI distribution function, (b) 2 ms after Tangential NBI turn-on, 10ms on/off period, (c) 2 ms after tangential NBI turn-on, tangential and perp NBI interleaved 10 ms on/off period. Note, in all cases only full-energy component is shown and arrow points to approximate avg. injected pitch.

feature created during beam modulation does not fulfill this assumption and can be a source of additional drive(21; 2).

Drive for higher frequency AEs such as compressional Alfvén eigenmodes (CAEs) and global Alfvén eigenmodes (GAEs) through velocity space anisotropies, as opposed to radial gradients, has received recent attention and even shown the stabilization of modes through flattening of these anisotropies(23; 22). At yet higher frequency, earlier work showed large fusion alpha orbits can create a bump-on-tail distribution in the edge and destabilize edge ion cyclotron emission (ICE)(24). In this work, the dependence of lower frequency modes such as BAEs, RSAEs and TAEs on beam modulation is

investigated during the current ramp phase of DIII-D discharges by varying beam modulation periods in a sequence of discharges with interleaved tangential and perpendicular beams. The resultant unstable mode activity is altered and, to a lesser degree, the mode driven fast ion transport. This paper is organized as follows. In Section 2, the basic discharge conditions, experimental approach and expected modification of the fast ion distribution function are presented. In Section 3, the experimentally observed variation in AE activity as beam modulation period is varied is presented. In Section 4, TRANSP kick modeling(25; 26; 27) and MEGA(28) simulations are used with experimental profiles to interpret the expected change in AE drive due to bump-on-tail effects, where it is concluded that bump-on-tail effects account for a relatively small portion of the drive for the most unstable mode observed.

## 2. DISCHARGE BACKGROUND AND EXPERIMENTAL APPROACH

The discharges presented in this paper utilize a standard DIII-D L-mode current ramp scenario for Alfvén eigenmode studies. In these $B_T = 2.15$ T discharges, 50-81 kV sub-Alfvénic neutral beam injection begins at $t = 300$ ms and continues while the plasma current ($I_p$) ramps up at a constant rate until reaching approximately 0.7 MA at $t = 1000$ ms. Time histories of plasma current, $q_{min}$, line-averaged electron density ($n_e$), central electron/ion temperature and injected neutral beam ($P_{NBI}$) for the primary discharges considered in this study are shown in Figure 2. The discharge itself is an upper single null ($\kappa = 1.79$, $\delta = 0.54$) with the upward bias used to avoid an H-mode transition. Electron temperature was diagnosed by a 40 channel electron cyclotron emission (ECE) diagnostic(40) as well as Thomson Scattering (which also measures electron density)(29; 30). Ion temperature and rotation were inferred through measurements of carbon impurities using charge exchange recombination spectroscopy (CER)(31). The safety factor profile was obtained using EFIT reconstructions constrained by a motional Stark effect (MSE) polarimetry system(32).

Early neutral beam injection during the current ramp phase typically produces a variety of Alfvénic activity in DIII-D plasmas including toroidicity induced Alfvén eigenmodes (TAEs)(33), reversed shear Alfvén eigenmodes (RSAEs)(34; 35), linearly coupled RSAEs and TAEs (36; 37), and beta induced Alfvén eigenmodes (BAEs)(38; 39). In this experiment, three beams were used, two "tangential" and one "perpendicular", the geometry of which are shown in Figure 3a. One of the tangential beams was fixed at 55 kV and, for diagnostic purposes, was injected
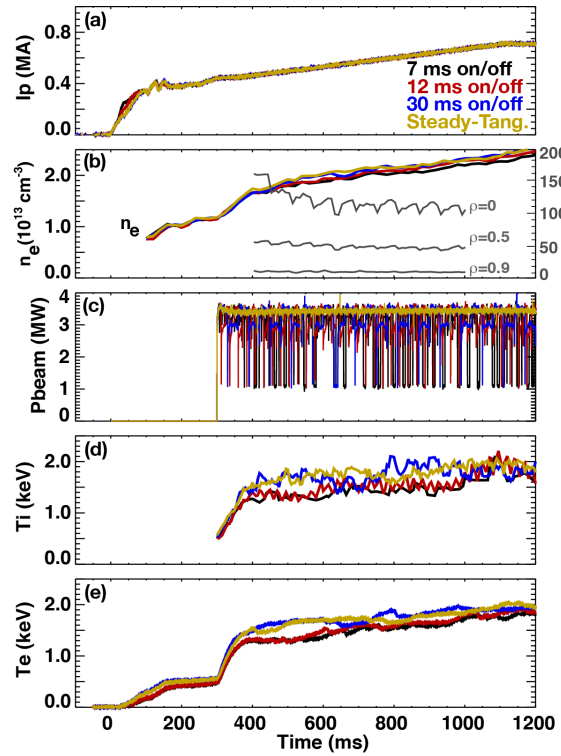


**Figure 2.** DIII-D discharges #176519, 176521, 176523 and 176525 with 7, 12, 30 ms on/off interleaving and a steady tangential beam respectively. (a) Plasma current, (b) line-averaged electron density overlayed with traces of full-energy slowing down times for 176523 at three different radii ($\rho = 0$, $\rho = 0.5$, $\rho = 0.9$), (c) Injected beam power, (d) ion temperature and (e) electron temperature near the magnetic axis.

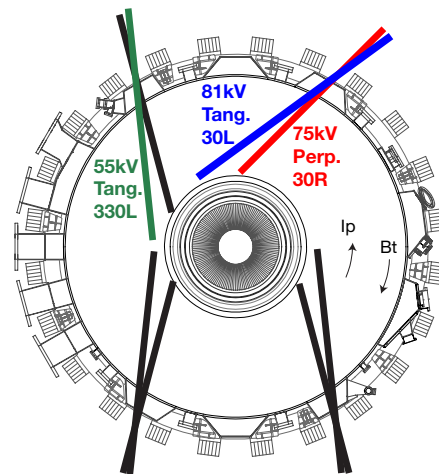steadily after $t = 300$ ms with approximately 40% of the power of the other beams. The other



**Figure 3.** DIII-D beam geometry. Beams used in this experiment are shown in color along with direction of plasma current and toroidal field. All beams are on plasma midplane.

two beams were fixed at 81 kV and 75 kV, for the tangential and perpendicular beams respectively, and
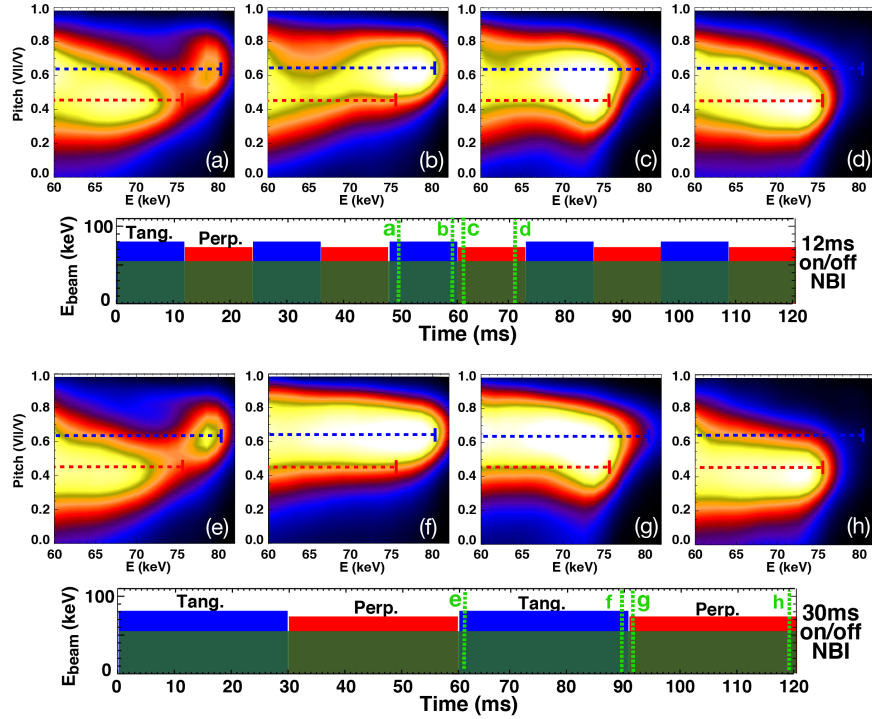
**Figure 4.** TRANSP calculated temporal evolution of the volume-averaged fast ion distribution function for: (a)-(d) 12 ms on/off interleaving and (e)-(h) 30 ms on/off interleaving of the 81 kV tangential and 75 kV perpendicular beams shown in Figure 3. The timing of the distribution function snapshots relative to the beam modulation are shown as dashed vertical lines overlayed on beam voltage waveforms.

are modulated out of phase with a modulation period that was varied from shot to shot to alter the bump-on-tail features and AE drive. Ideally both beams would be fixed at the same voltage, however, 81 kV is necessary for MSE data and 75 kV is the upper limit of the perpendicular beam. This difference also results in approximately 25% lower power from the perpendicular beam relative to the tangential. In a series of discharges, the modulation period was varied from 7 ms on/off to 30 ms on/off then a final discharge was carried out with a steady tangential beam. To put the modulation period in context, a typical slowing down time from 80 kV to 50 kV is approximately 20 ms. For all modulation cases, the overall time-averaged fast ion distribution function is similar. The temporal evolution of the kinetic profiles is also very similar as can be seen in Figure 2. The plasma current and electron density evolution is very well matched while the electron and ion temperature are both observed to be slightly higher for the 30 ms on/off and steady-tangential beam cases. This higher temperature could be a result of several factors, the first is that tangential beam is slightly higher power than the perpendicular so, for the steady beam case, more power is injected. Second, during beam modulation, each of the beams ramp up to full power over a period of approximately 10 ms, a consequence being that higher

time-averaged power is injected as the modulation period is increased. Third, the beam operation is slightly less reliable at the shortest modulation periods so, as the modulation period is decreased, occasionally some pulses are missed. Lastly, a variation in fast ion transport between the cases can result in a change in temperature.

The largest variation in the distribution function resulting from the different modulation periods and region of interest for bump-on-tail features occurs at highest energies, above that of the steady diagnostic beam. This can be seen in Figure 4, where the temporal evolution of the co-going portion of the distribution function above 60 kV is shown for 12 ms on/off and 30 ms on/off modulation periods. In Figures 4a - 4d, the temporal evolution at the beginning of each pulse in the 12 ms on/off modulation cycle is shown. At the beginning of the tangential beam pulse (Figures 4a), a bump-on-tail is formed at pitch $\chi \approx 0.65$ while the pulse at lower pitch ($\chi \approx 0.45$) has already begun to slow down away from the injection energy. By the end of the 12 ms tangential pulse (Figures 4b), the upper energy of the perpendicular beam feature has slowed to ~65kV and tangential beam has filled in down to 70 kV. At all times, a positive $\frac{\partial F}{\partial E}$ exists at the tangential beam pitch. After the tangential beam is turned off, it slows down and a

bump-on-tail feature forms at the pitch populated by the perpendicular 75 kV beam and the cycle largely repeats itself. At all times during the 12 ms on/off interleaving a region of positive $\frac{\partial F}{\partial E}$ exists at some pitch. For longer modulation periods, this is not the case. The evolution of the same region of velocity space during 30 ms on/off modulation is shown in Figures 4e-4h. For the 30 ms on/off interleaving, a bump-on-tail feature is initially formed at the injection pitch for each beam but the pulses are long enough such that a portion of each cycle has small or negative $\frac{\partial F}{\partial E}$ everywhere by the end of the 30 ms on periods.
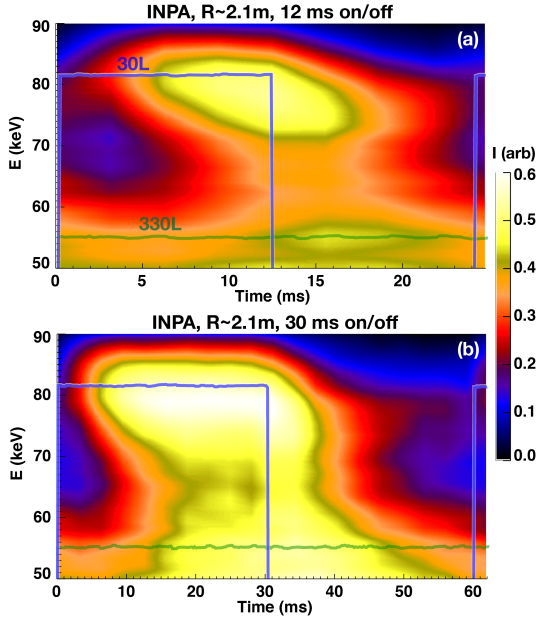


**Figure 5.** INPA scintillator data mapped to energy and time at $R \approx 2.1$ m and pitch$\approx 0.78$. Data are normalized by energy and are a coherent average of pulses over the interval $t = 419 - 517$ms and $t = 420 - 539$ms for (a) 12 ms on/off and (b) 30 ms on/off respectively. The 30L tangential (blue) and 330L tangential diagnostic beam (green) voltage waveforms are shown as overlays in both panels.

For these experiments, the Imaging Neutral Particle Analyzer (INPA)(4; 5; 6) was operated using a fast framing Phantom camera at frame rates up to 1 kS/s to resolve rapid changes to the local fast ion distribution function during the various modulation periods. The INPA probes the experimental fast ion distribution function at localized regions of velocity space across the plasma midplane corresponding to co-passing particles with $\chi \approx 0.7 - 0.8$ and confirms the expected bump-on-tail formation. Figure 5 shows the temporal evolution of the INPA data at $R \approx 2.1$ m (chosen due to proximity to the TAE discussed in Section 4 ) vs. energy for the 12 ms and 30 ms on/off modulation cases. The data presented in this figure are obtained by taking a coherent average over multiple 81 kV tangential beam pulses to lower

noise and are shown scaled by energy to remove the scintillator sensitivity, which is roughly proportional to energy(4). In each panel, the upper end of the 55 kV diagnostic beam (330L in Figure 3), is visible throughout the intervals shown. Immediately after turn-on of the higher energy tangential beam, signal at 81 kV appears, increases in magnitude and begins spreading to lower energy as beam ions slow down. Signal at energies above 81 kV is a result of both the diagnostic resolution, which is estimated to be $\delta E \approx 7.5$ kV, as well upscattering of the injected beam ions. For 12 ms pulses (Figure 5a), the signal and beam ion population at 81 kV continues to increase until the beam is turned off, at which point the upper energy beam ions slow down until the next pulse happens. Throughout the entire interval, some level of bump-on-tail is visible, particularly during the 81 kV tangential beam pulse. The 30 ms case (Figure 5b) is similar initially but eventually reaches a steady-state and higher level (i.e. higher beam ion density) at 81 kV and, by the end of the 30 ms beam pulse, has slowed and merged with the lower energy population created by the 55 kV diagnostic beam. Additionally, after turn-off, no significant bump-on-tail feature is apparent.

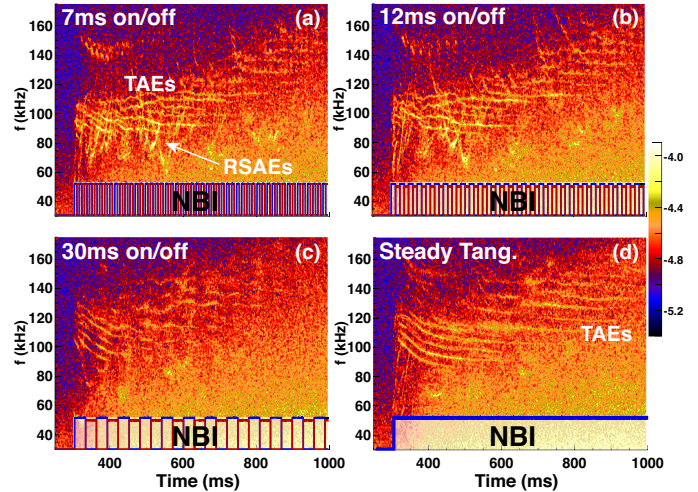## 3. IMPACT OF BEAM MODULATION PERIOD ON AE ACTIVITY



**Figure 6.** $CO_2$ interferometer crosspower spectrograms for (a) 7 ms on/off, (b) 12 ms on/off, (c) 30 ms on/off and (d) steady tangential beam.

A significant variation in Alfvén eigenmode activity was found as the beam interleaving was varied from shot to shot. A broad overview of the changes can be seen in Figure 6, where the crosspower of radial and vertical $CO_2$ interferometer chords(41) are shown for the different modulation periods along with the beam waveforms. As the interleaving is varied
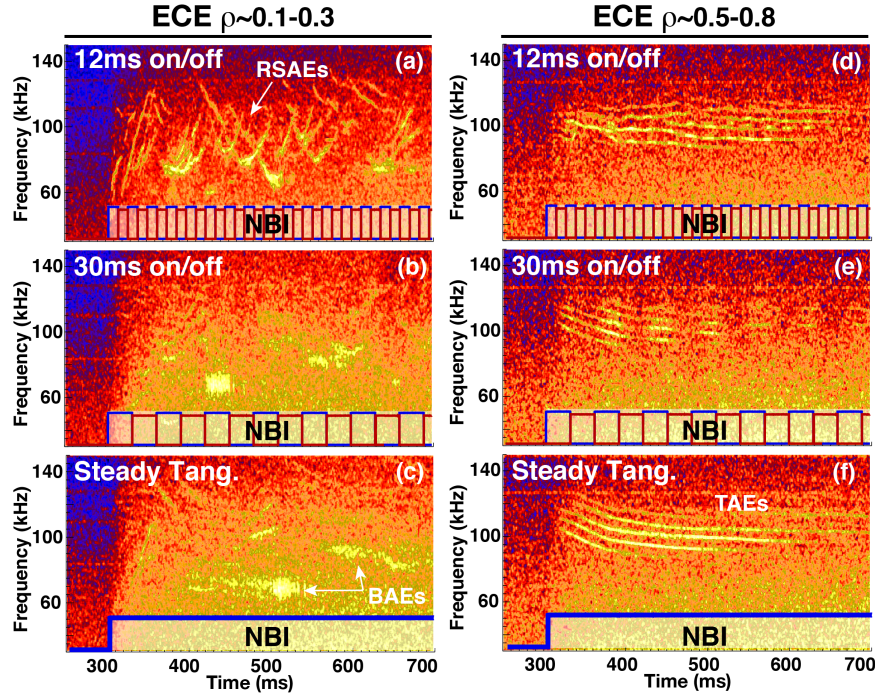
**Figure 7.** Spatially averaged ECE spectrograms for three different interleaving periods (12 ms on/off, 30 ms on/off and steady tangential beam) in two different radial regions. (a)-(c) $\rho \approx$ 0.2-0.4 and (d)-(f) $\rho \approx$ 0.6-0.8.

from 7 ms on/off to 30 ms on/off and eventually a steady tangential beam, the AE activity visible on the interferometers changes from a mix of RSAE and TAE to dominant TAE activity.

By looking at ECE data over select radial ranges, a local picture of how the mode activity varies with radius in response to the beam modulation is obtained(36). Figure 7 shows ECE spectrograms for the 12 ms, 30 ms and steady tangential beam cases in two different radial regions, $\rho \approx 0.2 - 0.4$ (Figure 7a-7c) and $\rho \approx 0.6 - 0.8$ (Figure 7d-7f). Starting at large radius (Figure 7d-7f), multiple TAEs are observed to be unstable in all cases. These modes are $n \approx 3 - 5$ (inferred from a toroidal array of Mirnov coils) and are strongest for the steady tangential beam case shown in Figure 7f. For the two interleaved cases, a modulation of the TAE amplitudes exist, however, they persist for the 12 ms case (Figure 7d) and are intermittent for the 30 ms on/off period (Figure 7e). This modulation of the TAE stability will be used in the next section to dissect the various contributions to mode drive. Further in, at radii near the shear reversal point (RSAE location), the mode activity is observed to change even more significantly. As the beam modulation period was increased to a steady tangential beam, the modes near $q_{min}$ change from a mix of predominantly RSAE with some indication of BAE activity (Figure 7a and 7b) to dominant BAEs in the steady tangential beam case (Figure 7c).

Figure 8 shows representative safety factor profiles along with ECE measured AE mode structures for the three cases. In all cases, the safety factor profiles have an off-axis minimum and are quite similar. The central q-value is elevated and the $q_{min}$location is at slightly smaller radius for the 12 ms case in comparison with the 30 ms on/off and steady tangential case. For the 12 ms on/off case an RSAE and TAE are shown and for the 30 ms on/off and steady tangential beam case, a BAE and TAE. The structure and frequency of the TAE is similar in all cases while the amplitude is the lowest for the 30 ms on/off case. As expected, the RSAE shown in Figure 8a is peaked near $q_{min}$, while the BAEs shown in Figures 8b and 8c are located inside of $q_{min}$.

While the change in TAE activity at large radius is understood and will be discussed in detail in Section 4, this shift in core activity is not currently understood. In all cases, the density and current evolution are well matched with slightly higher electron and ion temperatures in the 30 ms on/off and steady tangential beam cases (see Figure 2). Additionally, as shown in Figure 8, all cases have reversed magnetic shear. A detailed analysis of BAE activity in DIII-D is currently underway and will be the subject of future publications(43); however, a large database study indicates BAE tend to be destabilized preferentially by tangential beams(42). This can certainly be the cause for the steady tangential beam case but it is not as clear
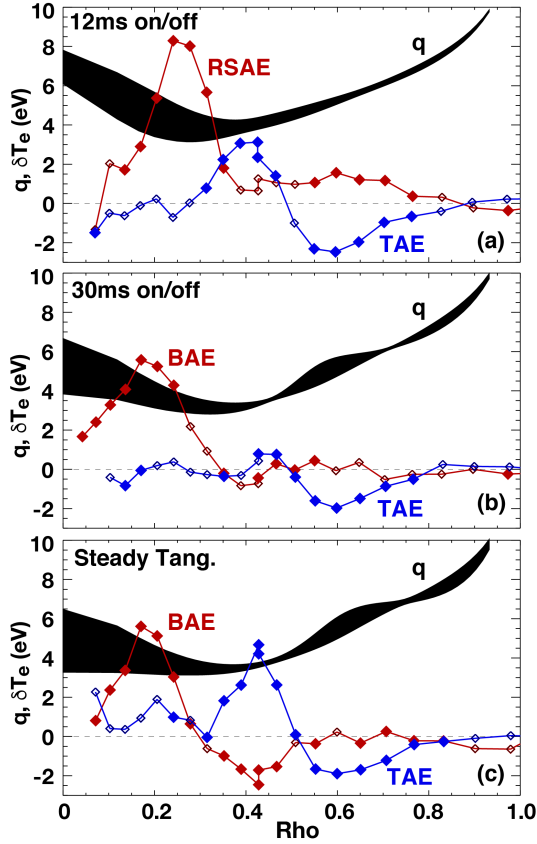
**Figure 8.** Safety factor profile and example mode structures for 12 ms on/off, 30 ms on/off and steady tangential beam. a) $t_{efit} = 645$ ms, $f_{RSAE} = 98$ kHz, $f_{TAE} = 109$ kHz, b) $t_{efit} = 615$ ms, $f_{BAE} = 86$ kHz, $f_{TAE} = 103$ kHz, c) $t_{efit} = 615$ ms, $f_{BAE} = 88$ kHz, $f_{TAE} = 113$ kHz. Mode structures are $\delta T_e$ on outboard midplane. Filled diamonds indicate coherence relative to peak above 95% conf. level.

when interpreting the shift with modulation period, although long on-periods are classically expected to create higher peak populations of the relevant fast ions, something that is observed with the INPA (Figure 5). In the same study(42), BAEs were found to decay more rapidly than RSAEs after beam turn-off, indicating they were driven by higher energy particles. The tangential beam used here is significantly higher energy than the perpendicular (81 kV vs. 75 kV). The database investigation of BAE stability also indicates that the modes are destabilized more easily at higher beta(42; 43), thus, the higher $T_e$ and $T_i$ at fixed density may also contribute to the shift from RSAE to BAE. It is noted that this shift from RSAE to BAE is not a common observation on DIII-D; in fact BAEs are not as common as RSAEs and TAEs, whereas TAE modulation, like that observed at larger radii, is more frequently observed.

Figure 9 focuses on the evolution of the TAE instabilities during beam modulation for the 30 ms on/off case. Figure 9a shows the mode activity as
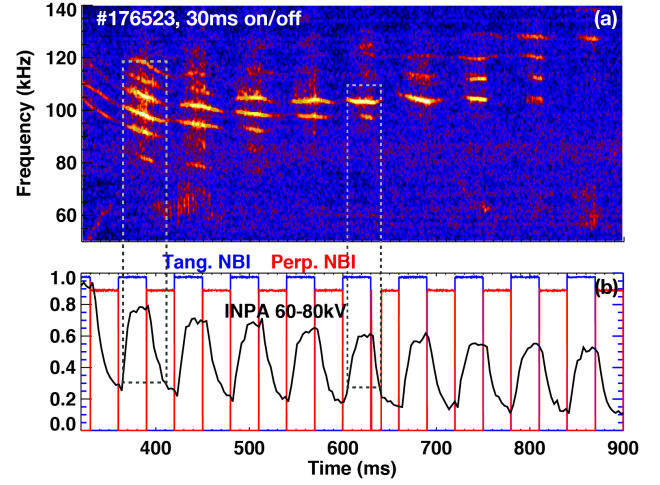


**Figure 9.** (a) Magnetics spectrogram for 30 ms on/off interleaving. (b) Beam waveforms overlayed with raw INPA signal near TAE location integrated over $E = 60 - 80$ kV.
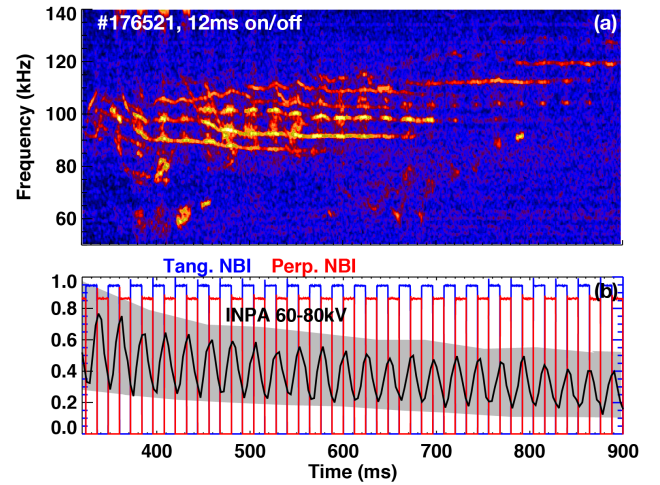


**Figure 10.** (a) Magnetics spectrogram for 12 ms on/off interleaving. (b) Beam waveforms overlayed with raw INPA signal near TAE location integrated over $E = 60 - 80$ kV. Shaded region is INPA modulation envelope from 30 ms on/off case (Figure 9b).

measured by edge magnetic probes and Figure 9b shows the beam waveforms along with data from the INPA. Immediately obvious from this and Figure 7 is the fact that TAEs are preferentially driven by the tangential beam. The INPA probes the region of velocity space populated by the tangential beam and the data shown in Figure 9b for any given beam pulse are roughly proportional to the co-going passing particle fast ion density near the TAE location integrated between 60-80 kV. The overall downward drift is due to sensitivity of the diagnostic to density, resulting from the reduction in neutral penetration and escaping neutral flux. At each tangential beam pulse, the INPA signal increases, reaches a plateau and

decreases exponentially after the tangential beam turn-off. Individual TAEs were found to be destabilized at each tangential beam pulse with instability setting in at increasingly longer delays after beam turn-on (i.e. higher local fast ion density) and becoming stable sooner after turn-off as the minimum safety factor decreases. This effect is explained by reduced coupling to side-band resonances(44) and reduced drive efficacy as $q_{min}$ decreases. A complementary plot is shown in Figure 10, where the 12 ms data are displayed. In this case, the TAEs still clearly rise to peak amplitude during tangential beam pulses; however, the majority of TAEs remain unstable and persist even between tangential pulses when the perpendicular beam is on. Also apparent is that the INPA data do not plateau as in the 30 ms case (Figure 9b). In fact, the INPA data do not rise nor fall to the extremes reached in the 30 ms case, as can be seen by comparing the INPA data in Figure 10b to the overlayed shaded region which represents the amplitude envelope of the 30 ms INPA data. Evidently, the driving fast ion density (or gradient) doesn't decay enough between pulses to reduce the drive sufficiently and the TAE remains unstable. An interesting question is whether the intermittent TAEs in the 30 ms case, despite possibly being driven more strongly during on-periods of the tangential beam, should be expected to cause more or less fast ion transport than the shorter modulation period (7 or 12 ms) in which TAEs persist throughout the current ramp. In all modulation cases, the time-averaged power is approximately the same.

As the modulation period was varied, the AE impact on fast ion confinement was also found to vary slightly. To assess the fast ion transport, both neutron emission and stored energy are compared to classical TRANSP predictions. A difference in DD neutron emission and/or stored energy relative to TRANSP calculations, which assume neoclassical confinement, indicates larger than expected fast ion transport and is weighted towards higher energies. The actual measured neutron rates have an uncertainty of approximately 15%, however, the relative error in a comparison of two separate discharges is significantly smaller(45). Figure 11 shows a large deficit in neutron emission (Figure 11b) and stored energy (Figure 11c) for all modulation periods. Early during the current ramp, the central fast ion deficit is large, with 50-60% of the classically expected neutron emission and 20% deficits in stored energy, both of which return to near classical levels after approximately $t = 1100$ ms. For a given level of fast ion transport, the relative stored energy deficit is smaller due to the fact that the majority of the equilibrium pressure is from the thermal plasma. Also apparent from Figure 11 is the fact that all modulation periods exhibit similar

levels of fast ion transport. An estimate for the global amplitude of AE activity in the various cases is also shown in Figure 11a, where the integrated power of density fluctuations from the CO2 interferometer in the AE frequency band with high coherence between chords is given. Of all cases, the 30 ms interleaving case, which has intermittent TAEs at large radii and a mixture of weaker RSAE and BAE activity in the core, has approximately the lowest "mode amplitude", and lowest fast ion transport on average. Relative to the 7 ms modulation period, the neutron deficit for the 30 ms case varies from 25-40% lower depending on time in the current ramp.
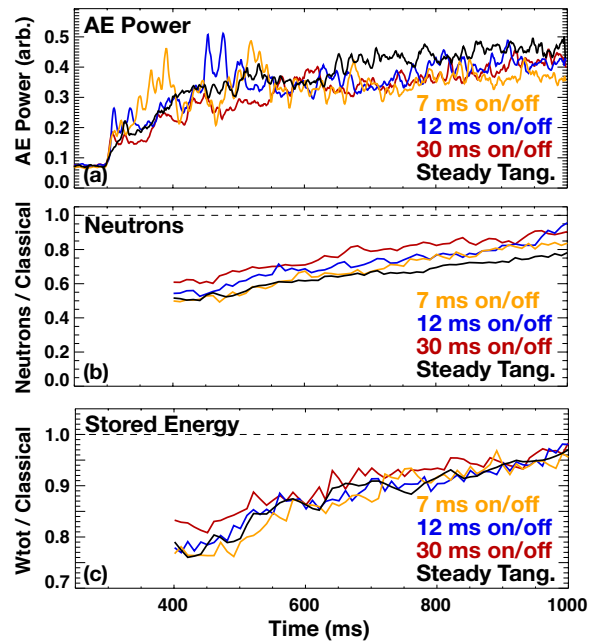


**Figure 11.** Data for 7, 12, 30 ms on/off interleaving and a steady tangential beam. (a) Integrated power in AE frequency band from CO2 interferometer crosspower. (b) Neutron emission relative to classical TRANSP predictions. (c) Stored energy relative to classical TRANSP predictions. Note suppressed zero for stored energy plot.

## 4. MODELING AND ANALYSIS OF BUMP-ON-TAIL CONTRIBUTIONS TO AE DRIVE

The TAE modulation shown in Figure 9 provides a useful dataset for assessing the degree to which the bump-on-tail features play a role in the mode's stability. As will be shown, TAEs are driven by the highest energy portion of the distribution function, which is also where the bump-on-tail features appear. To get an idea how the driving energy gradient changes with respect to mode evolution, a single tangential beam pulse is focused on in Figure 12. Here, the TRANSP calculated distribution function near the
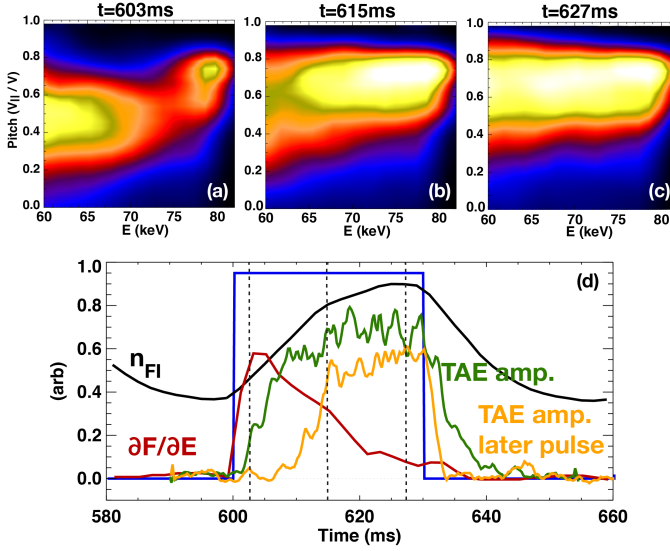
**Figure 12.** (a)-(c) Evolution of TRANSP calculated distribution function near TAE for 30 ms on/off case. (d) Fast ion density between 60-85 kV near tangential beam pitch (black), maximum energy gradient near tangential beam pitch (red), TAE amplitude (green), TAE amplitude from subsequent pulse (yellow).

TAE location is shown at the beginning, middle and end of the tangential beam pulse in Figures 12a-c. In Figure 12d, the temporal evolution of the maximum energy gradient is given along with the local fast ion density at the tangential beam pitch and TAE amplitude evolution. From this figure, it is clear the TAE amplitude follows the local fast ion density (and thus radial gradient at pitch populated by beam) far more closely than the positive energy gradient. In fact, the TAE amplitude doesn't begin to decay until the beam is turned off and the density begins to decay. This is long after the maximum energy gradient is $< 10\%$ of its peak. To further show the relative insensitivity to the energy gradient, the TAE amplitude at a subsequent pulse is also overlayed. In this case, the TAE doesn't even become unstable until after the energy gradient is decreasing, approximately 5-10 ms after its peak. While not quantitative, this analysis appears to indicate the energy gradient is not the primary drive source for the TAEs.

### 4.1. TRANSP Kick Modeling

To more quantitatively assess the fractional contribution to TAE drive due to bump-on-tail features and the temporal evolution during beam pulses, the kick model(25; 26; 27) in TRANSP(3) was used in a numerical experiment with the experimental conditions from Figure 12. First, the ideal MHD eigenmodes were calculated using the NOVA code(46; 47) and a single $n = 3$ TAE corresponding to that in experiment was

found (see Figure 13a). Next, the "kick probability" matrices, which give the phase space dependent energy exchange for this mode, were calculated with the ORBIT code(48). This kick matrix, shown in Figure 13b for the full injection energy, was then used as an input to TRANSP. In the numerical experiment, the equilibrium conditions were held fixed and a 300 ms (several slowing down times) series of tangential and perpendicular beam pulses analogous to those in the experiment were injected in the presence of the mode while tracking the energy exchange with the mode. Four beam scenarios were considered: 1) steady tangential beam, 2) steady perpendicular beam, 3) interleaved tangential and perpendicular beams with 12 ms on/off periods and 4) 30 ms on/off periods. The actual TAE amplitude was held fixed and set to a low value to cause negligible redistribution while being able to track the energy exchange. An example of the temporal evolu-
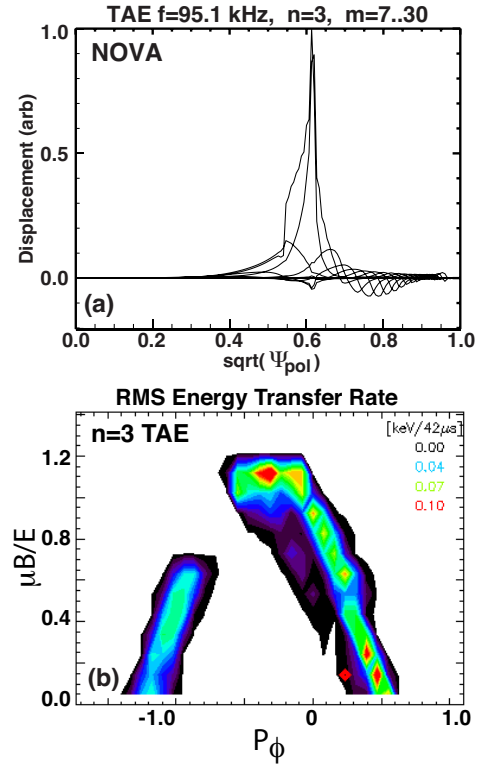


**Figure 13.** (a) $n = 3$ NOVA calculated TAE corresponding to experimental TAE in 176523 at $t \approx 615$ ms used in kick modeling. (b) Example TAE kick matrix at full energy. $P_\phi$ = toroidal canonical angular momentum normalized by the poloidal flux ($\Psi_{pol}$) at the last closed flux surface, $\mu$ = magnetic moment, $B$ = toroidal field, $E$ = particle energy (80kV).

tion of the power to the TAE for the 12 ms on/off case is shown in Figure 14. The simulation begins with a monotonically increasing power transfer as the fast ion population is built up over a slowing down time then, after $\approx 60$ ms, a relatively steady-state is reached and the power to the TAE (Figure 14a) can be seen to os-

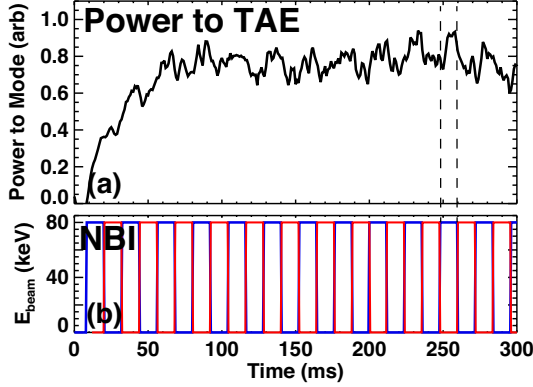cillate roughly with a timescale similar to the beam interleaving (Figure 14b).



**Figure 14.** (a) Kick model simulations of power transfer to TAE for beam modulation voltage waveforms shown in (b). Perp/Tang. beams are red/blue.

The average power transfer for each of the four cases is shown in Figure 15a, where the average is taken after $t = 100$ ms. The simulation confirms the experimental observation that the tangential beam is more effective at driving the TAE, with more than twice the power transfer to the mode than the perpendicular beam. A similar result was found in previous experiments which scanned beam power from tangential to perpendicular(49). The simulation also shows that, in a time averaged sense, the power transfer to the mode is independent of the modulation period for the two values used (12 and 30 ms on/off), and that the average power transfer is approximately the average of that from the two independent beams. The fact that these are the same, despite the differences in bump-on-tail features is consistent with a small energy-gradient contribution to the drive. While the temporal evolution of the power transfer to the TAE is relatively noisy during any individual beam pulse, a coherent average over beam pulses reveals the dynamics of the power transfer as one beam slows down and the other builds up and the bump-on-tail features evolve. Coherent averages during a tangential and perpendicular beam cycle for the 12 ms on/off and 30 ms on/off cases are shown in Figures 15b and 15c respectively. For the 12 ms case, the coherent average waveform is repeated so it can be plotted on the same timescale as the 30 ms case. For the 12 ms case, the power to the TAE increases throughout the tangential beam pulse then decays rapidly during the perpendicular beam phase. The rapid $\approx 4$ ms decay indicates the highest energy tangential beam ions are most effective at driving the mode. For the 30 ms case, the power transfer rises rapidly then decreases by approximately 5% until a steady-state is reached at roughly 13 ms after the tangential pulse turns on. As in

the 12 ms case, after the tangential pulse turns off, the power transfer decays rapidly. The transient dynamics of the power exchange during the initial turn-on of the tangential beam in the 30 ms case (Figures 15c) is illuminating in that the 5% difference between the peak at $t \approx 7$ ms and the steady state at 13+ ms is likely an indication of the bump-on-tail contribution to the drive. As shown in Figure 12a-c, this is the timescale over which we can expect the positive energy gradient of the bump-on-tail feature to exist.
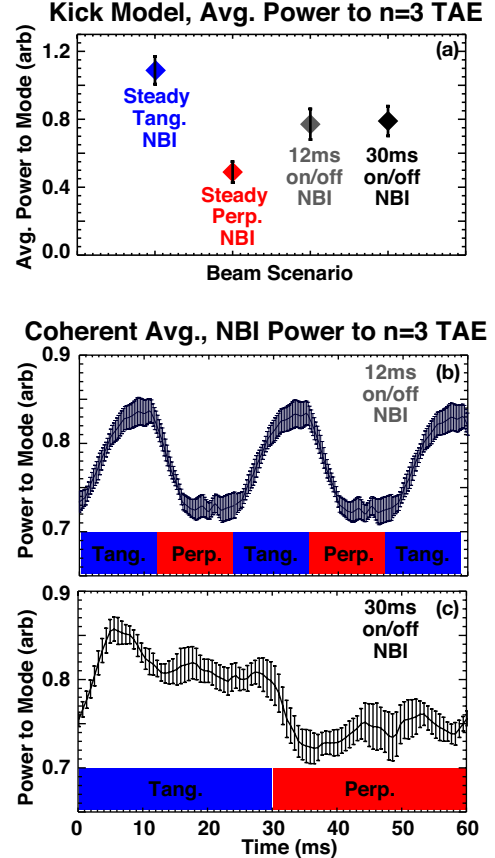


**Figure 15.** Kick model calculations. (a) Time averaged power to the TAE for four different beam scenarios. (b) & (c) power to mode obtained by coherent average of several beam cycles for 12 ms and 30 ms on/off interleaving.

### 4.2. MEGA Modeling

In a addition to TRANSP kick modeling described in the previous section, MEGA simulations were used to more systematically model the impact of a bump-on-tail fast ion distribution function on AE stability. MEGA is a hybrid kinetic-MHD code, that includes energetic particles(28), which has successfully modeled AE stability and transport in DIII-D scenarios like those presented here(50; 51; 52). For this application, fast ions were included using a $\delta F$ Particle-in-Cell approach for the gyrokinetic markers with an
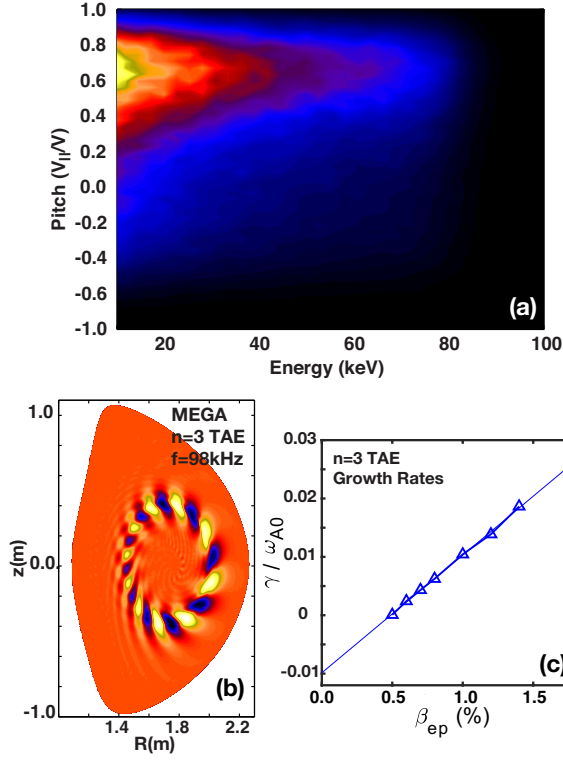
**Figure 16.** (a) Approximate beam-like distribution function used in MEGA for tangential beam. (b) Most unstable mode for experimental conditions corresponding to 30 ms on/off interleaving case 176523 at $t \approx 615$ ms. (c) TAE growth rate as central fast ion beta is scaled. Experimental $\beta_{ep} \approx 0.7\%$



**Figure 17.** (a) Beam-like distribution function with bump-on-tail feature used in MEGA simulations. (b) line-slice at beam pitch through distribution function in panel (a). Arrows show adjustable bump-on-tail parameters.



**Figure 18.** MEGA results for bump-on-tail scan. (a) Range of gradients used at constant peak value. (b) Range of peak values used at constant gradient. (c) Contour of $n = 3$ TAE growth rates for bump-on-tail scan. (d) Mode energy evolution for all cases.

anisotropic slowing down form for the distribution function prescribed. The same equilibrium and kinetic profiles used for TRANSP kick modeling have been employed here. An example volume averaged slowing down distribution function for a steady tangential beam is shown in Figure 16a and the unstable $n = 3$ TAE that was found in the simulation is shown in Figure 16b along with the growth rates as a function of fast ion beta $\beta_{ep}$ in Figure 16c. Encouragingly, the $n = 3$ TAE is the most unstable mode and is very similar to that found in experiment and identified in NOVA. Also similar to experiment, the TAE growth rate decreases significantly when the injected pitch was modified to be that of the more perpendicular beam.

For this study, the effects of a bump-on-tail at the injection energy were included in MEGA with a model distribution that consists of a Gaussian added to the standard anisotropic slowing down distribution. The features are set by specifying the standard slowing down distribution parameters as well as a peak and gradient value of the bump-on-tail. An example input slowing down distribution with combined bump-on-tail is shown in Figure 17a along with a slice at the injection pitch in Figure 17b. In a series of systematic scans, the bump-on-tail peak and gradient were varied over
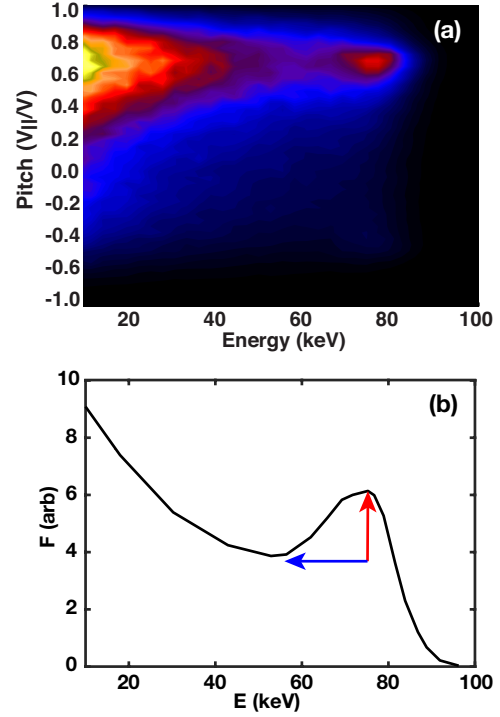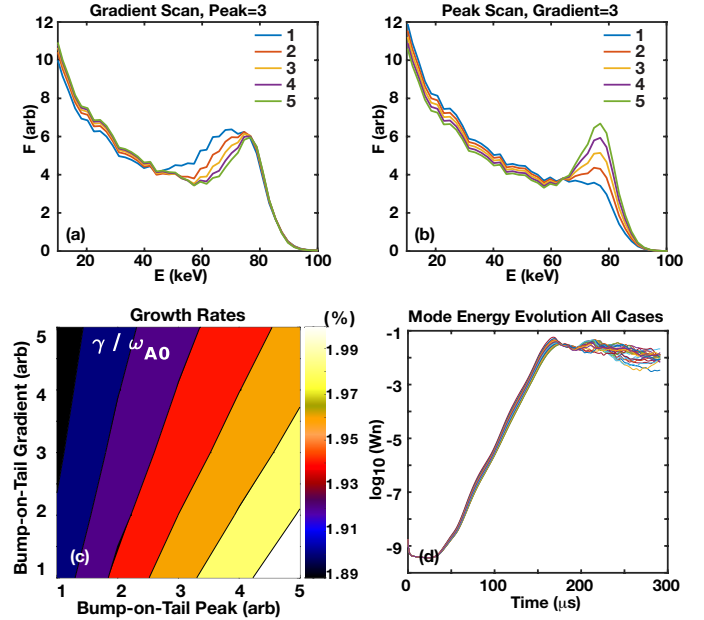
the ranges shown in Figure 18a and Figure 18b, while holding the total fast ion pressure profile fixed, and

the impact on $n = 3$ mode stability investigated. In all cases, the same TAE was found to be the most unstable mode with the variation in growth rate of the mode shown in Figure 18c as a function of bump-on-tail peak and gradient. The actual mode energy evolution for all cases is shown in Figure 18d. Despite the large variation in bump-on-tail parameters, the mode energy evolution and inferred growth rates vary rather weakly with only a 5.5% variation over the entire range. As the peak increases, for a fixed gradient scale, the growth rate increases as expected. As the gradient increases for a fixed peak value, the growth rate actually decreases slightly, which is somewhat counterintuitive. It is possible this effect is a result of the fact that, as implemented, the increased gradient actually comes at the expense of decreasing the portion of phase space over which the positive energy gradient exists and actually increasing the extent of the typical slowing down negative energy gradient. Nonetheless, this relatively minor change in growth rate due to a bump-on-tail feature in addition to that from the anisotropic beam-like distribution is consistent with that inferred from the TRANSP kick modeling (see discussion of Figure 15c).
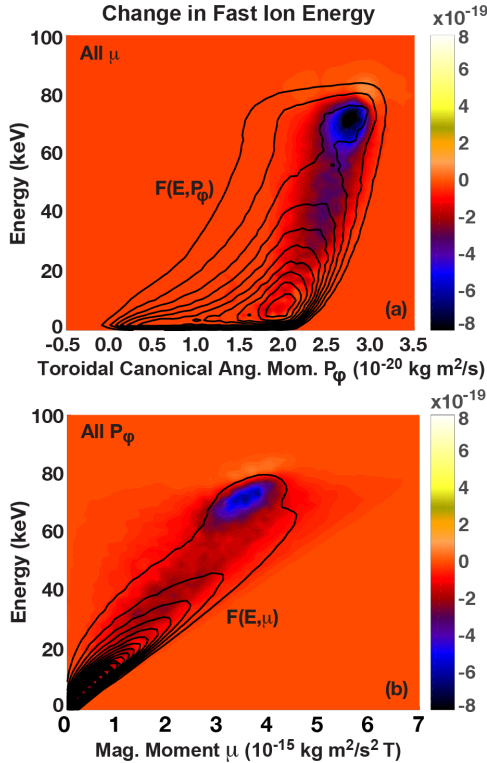


**Figure 19.** Color contour is change in fast ion energy and black contours are distribution function. (a) Integrated over $\mu$, (b) Integrated over $P_\phi$

The primary reasons contributing to the magnitude of the bump-on-tail effect on TAE stability are revealed by tracking the energy exchange in MEGA. The energy exchange between the fast ions and AE as a function of toroidal canonical angular momentum and energy integrated over magnetic moment is shown in Figure 19a, and as a function of magnetic moment and energy integrated over $P_\phi$ in Figure 19b. Overlayed on the figure are contours of the distribution function with an obvious bump-on-tail feature near $P_\phi = 2.7 \times 10^{-20}$ kg m$^2$/s in Figure 19a. Negative values of fast ion energy exchange correspond to mode drive and positive to mode damping. Clearly more energy is given to the mode than is lost to it, resulting in mode growth. The largest energy exchange occurs near the injection energy and between approximately 60-80 kV. This contributes to the observed rapid mode decay when the tangential beam was turned off in both experiment and the TRANSP kick modeling.
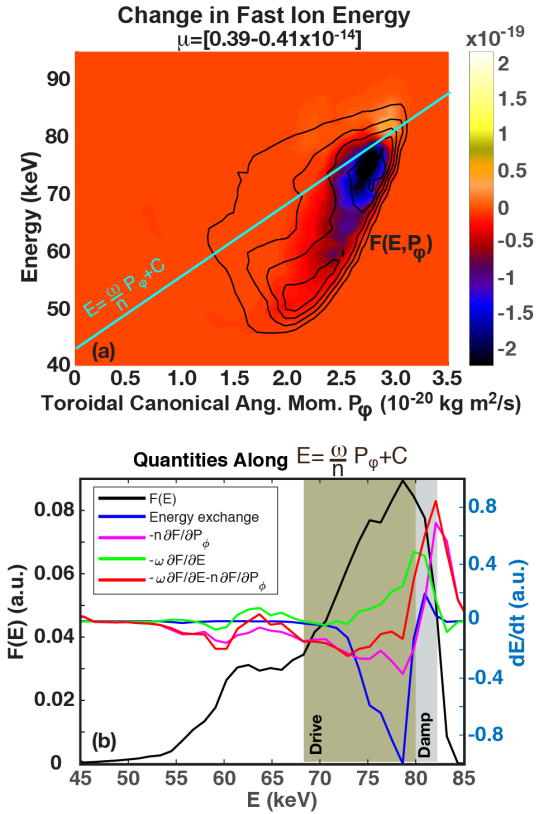


**Figure 20.** (a) Color contour is change in fast ion energy and black contours are distribution function for $\mu$=0.39-0.41$\times10^{-14}$ kg m$^2$/s$^2$T. (b) Line plots taken along $E = \omega/nP_\phi + C$ from panel (a). $F(E)$ uses left axis, all others use $dE/dt$ axis on right.

Figure 20a shows the energy exchange in the $\mu$ range corresponding to the peak of that in Figure 19b plotted as a function of $P_\phi$ and energy. Overlayed is a line corresponding to $E = \omega/nP_\phi + C$, where $C$ is a constant chosen to intersect a region with positive and negative energy exchange for illustrative purposes.
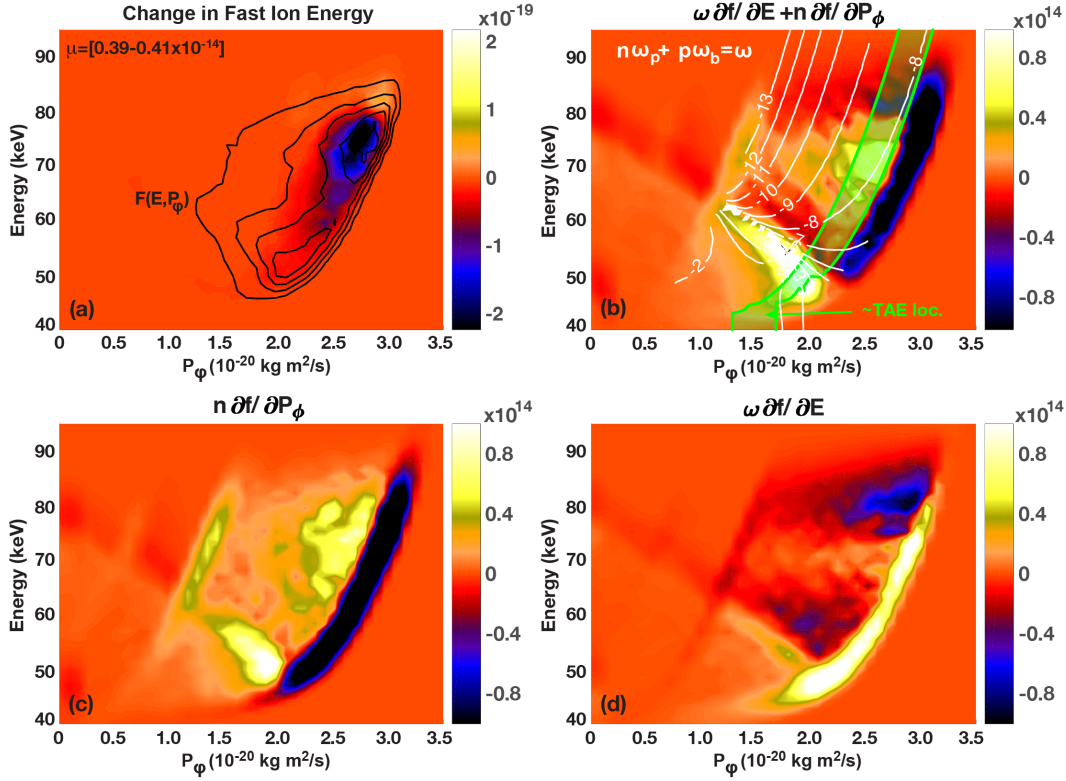
**Figure 21.** a) Color contour is change in fast ion energy and black contours are distribution function for $\mu$=0.39-0.41$\times 10^{-14}$ kg m$^2$/s$^2$T. (b) Combined gradient contributions to growth rate. White contours are resonances with the $n = 3$, $f = 98$ kHz TAE, where the corresponding integer $p$ is labelled. Green shaded region represent orbits overlapping approximate mode location. (c) $P_\phi$ gradient and (d) $E$ gradient. It is noted that the largest gradients apparent in panels (a)-(d), along the large $P_\phi$ side of the distribution, are not responsible for appreciable drive or damping, as this corresponds to the magnetic axis.

This line corresponds to the direction of motion particles make in the $P_\phi, E$ plane in the presence of the $n = 3$ TAE and the direction over which gradients in $E$ and $P_\phi$ must be evaluated for their contribution to mode drive.(20) Figure 20b shows the relevant quantities evaluated along the $E = \omega/nP_\phi + C$ line from Figure 20a. By comparing energy exchange (blue) with the distribution function, it's clear the negative energy exchange (mode drive) corresponds to regions of positive gradient whereas positive (mode damping) to regions of negative gradient. In a tokamak, for low frequency modes such that $\mu$ is conserved, the energy transfer is proportional to(19)

$$\gamma \propto \omega \frac{\partial F}{\partial E} + n \frac{\partial F}{\partial P_\phi}. \tag{1}$$

To separate the two contributions, the actual $E$ and $P_\phi$ gradients are also shown in Figure 20b as well as their combination scaled by $\omega$ and $n$ respectively. Along this slice through velocity space, $\frac{\partial F}{\partial E}$ essentially only contributes to mode damping while the mode drive is supplied by $\frac{\partial F}{\partial P_\phi}$.

The relative contributions of the two driving gradients are clarified further in Figure 21. In Figure 21a, the change in fast ion energy from

Figure 20a is shown. In Figure 21c and Figure 21d, the contribution from $n\frac{\partial F}{\partial P_\phi}$ and $\omega\frac{\partial F}{\partial E}$ respectively are shown in the $P_\phi, E$ plane. It is noted that the largest gradients apparent in both figures along the large $P_\phi$ side of the distribution are not responsible for appreciable drive or damping, as this corresponds to the magnetic axis. In the region of largest fast ion energy change ($P_\phi, E \approx [2.6\times 10^{-20}$ kg m$^2$/s, 73 kV]), the $P_\phi$ gradient contribution is significantly larger than that from the bump-on-tail positive energy gradient ($E \approx 65 - 75$kV). At energies above the injection energy ($E >80$ kV) the energy gradient contribution provides significant damping. The combination of the two are shown in Figure 21b, overlayed with resonance contours as well the region of phase space overlapping with the approximate TAE location. Here, the TAE location highlighted corresponds to $E$ and $P_\phi$ of particles with $\mu = 0.39-0.41\times 10^{-14}$ kg m$^2$/s$^2$T that intersect the TAE radial location along the outboard midplane. The resonance contours are defined by:

$$n\omega_p + p\omega_b = \omega, \tag{2}$$

where $\omega_p$ is the toroidal precession frequency, $\omega_b$ is the poloidal bounce frequency, $\omega$ is the TAE angular frequency and $p$ is an integer.(19; 20)

For energy exchange to take place, and enhancement of mode growth rates to occur, a few conditions must be satisfied. First, a resonance must be in the positive gradient region ($E$ and/or $P_\phi$), and second, the mode must overlap with particle orbits in that part of phase space. In general, simply having a positive energy gradient somewhere in the distribution function is not sufficient for mode drive; the modes must be able to tap the free energy available in this gradient through resonant interactions. The strength of the interaction is governed by the order of the resonance. For the $m = 9, 10, n = 3$ TAE, the $p = -8$ resonance goes through the largest regions of drive overlapping with the mode location. The resultant energy exchange shown in Figure 21a is a combination of these different effects with the result being that the largest fraction of the drive comes from the $\frac{\partial F}{\partial P_\phi}$ contribution and some damping due to the rapid drop off of the distribution function above the injection energy (negative $\frac{\partial F}{\partial E}$ is also apparent. The importance of the damping above the injection energy is likely the reason for the modest change in mode growth as the peak of the bump-on-tail feature is increased, i.e. both the energy gradient drive below the injection energy and the damping compete with each other. This large contribution to the damping may, in fact, offer control possibilities. Through judicious choice of injection energy (or energies), one could envisage placing the upper energy damping such that it intersects with the lowest order resonance available.

## 5. SUMMARY AND CONCLUSIONS

Results from a recent DIII-D experiment investigating the impact of neutral beam modulation period on AE activity have been presented. In the experiment, two different geometry beams were interleaved with a modulation period that varied from shot to shot in order to modify the relative time dependent mix of the beam pitch angle distribution as well as the persistence of a bump-on-tail feature near the injection energy. Significant differences in Alfvén eigenmode activity and EP transport for the same time-averaged injected power but different modulation periods are found. As the beam modulation period is varied from 7 ms to 30 ms on/off (typical full energy slowing down time of $\tau_{slow} \approx 50$ ms at mid-radius), TAEs located in the outer periphery of the plasma become intermittent and coincident with the more tangential beam. Core mode activity changes from RSAE to a mix of RSAE and BAE. Discharges with 30 ms on/off period do not have a persistent bump-on-tail feature, have the lowest average mode amplitude and least fast ion transport. Detailed analysis of an individual TAE using TRANSP kick modeling and MEGA find no strong role of energy gradient drive due to bump-on-tail features and that the observed TAE modulation with interleaved beams is likely a pitch angle dependent result combined with slowing down of the tangential beam between pulses. For the conditions investigated, bump-on-tail contributions to TAE drive were found to be at most 5% of the total drive at any given time.

Core mode activity was observed to shift from RSAE to weaker RSAE and BAE activity as the interleaving modulation period was increased. An initial analysis with NOVA did not find a BAE for analysis and the version of MEGA employed cannot find BAEs. This shift is not currently understood although it may be due to either the higher energy of the tangential beam and/or the increased thermal plasma beta in cases where the shift is observed. Nonetheless, this shift is difficult to interpret with the available tools and will be the subject of future investigations. Future work will also include a focused analysis of the nonlinear evolution and saturation of individual TAEs such as that shown in Figure 12.

For scenarios in which maximum beam power is not required, these results indicate that fine-scale tailoring of beam modulation, injection energy and interleaving of different beams may offer additional opportunities for instability control.

## 6. Acknowledgements

those of the United States Government or any agency thereof.

## References

[1] Landau, L.D. *Zh. Eksp. Teor. Fiz.* **10**, 25 (1946).

[2] Ya.I. Kolesnichenko and V.V. Lutsenko *Nucl. Fusion* **59**, 126005 (2019).

[3] Poli, Francesca, Sachdev, Jai, Breslau, Joshua, Gorelenkova, Marina, Yuan, Xingqiu. (2018, Oct 7). TRANSP v18.2. [Computer software]. doi:10.11578/dc.20180627.4.

[4] X.D. Du, M.A. Van Zeeland, W.W. Heidbrink and D. Su *Nucl. Fusion* **58**, 082006 (2018).

[5] M.A. Van Zeeland, X.D. Du, W.W. Heidbrink, L. Stagner and D. Su *JINST* **14**, C09027 (2019).

[6] X.D. Du, M.A. Van Zeeland, W.W. Heidbrink, L. Stagner, A. Wingen, D. Lin, and C.S. Collins *Nucl. Fusion* **In Press** (2020).

[7] H.H. Duong, W.W. Heidbrink, T.W. Petrie, R. Lee, R.A. Moyer, J.G. Watkins, *Nucl. Fusion* **33**, 749 (1993).

[8] W.W. Heidbrink, et.al. *Phys. Rev. Letters* **99**, 245002-1 (2007).

[9] M. Garcia-Munoz, I.G.J. Classen, B. Geiger, W.W. Heidbrink, et.al. *Nucl. Fusion* **51**, 103013 (2011).

[10] C.T. Holcomb, et.al. *Phys. Plasmas* **22** 0555904 (2015).

[11] C.S. Collins, W.W. Heidbrink, et.al. *Phys. Rev. Letters* **116**, 095001 (2016).

[12] M.A. Van Zeeland, et.al. *Phys. Plasmas* **18** 056114 (2011).

[13] G.J. Kramer, M. Podesta, C. Holcomb, et.al. *Nucl. Fusion* **57**, 056024 (2017).

[14] shikawa, M. and Takechi, M. and Shinohara, K., et.al. *Nucl. Fusion* **47**, 849 (2007).

[15] Nabais, F. and Kiptily, V. G. and Pinches, S. D. and Sharapov, S. E., et.al. *Nucl. Fusion* **50**, 084021 (2010).

[16] Gassner, T. and Schoepf, K. and Sharapov, S. E. , et.al. *Phys. Plasmas* **19**, 032115 (2012).

[17] R. B. White, E. Fredrickson, D. Darrow, M. Zarnstorff, R. Wilson, S. Zweben, K. Hill, Y. Chen, and G. Fu *Phys. Plasmas* **2** 2871 (1995).

[18] M.N. Rosenbluth and P.H. Rutherford *Phys. Rev. Letters* **34**, 1428 (1975).

[19] W.W. Heidbrink *Phys. Plasmas* **15** 055501 (2008).

[20] Todo, Y. *Rev. Mod. Plasma Phys.* **3** 1 (2019).

[21] V.S. Belikov and O.A. Silvra *Nucl. Fusion* **34** 1522 (1994).

[22] Fredrickson, E. D. and Belova, E. V. and Battaglia, D. J., et.al. *Phys. Rev. Letters* **118** 265001 (2017).

[23] Bortolon, A. and Heidbrink, W. W. and Kramer, G. J. and Park, J.-K. and Fredrickson, E. D. and Lore, J. D. and Podesta, M. *Phys. Rev. Letters* **119** 265008 (2013).

[24] Cottrell, G. A. and Bhatnagar, V. P. and da Costa, O., et.al. *Nucl. Fusion* **33** 1365(1993).

[25] M. Podesta, M. Gorelenkova and R.B. White *Plasma Phys. Control. Fusion* **56** 055003 (2014).

[26] M. Podesta, M. Gorelenkova, E.D. Fredrickson N.N. Gorelenkov and R.B. White *Nucl. Fusion* **56** 112005 (2016).

[27] M. Podesta, M. Gorelenkova, N.N. Gorelenkov and R.B. White *Plasma Phys. Control. Fusion* **59** 095008 (2017).

[28] Todo Y. and Sato T., Phys. Plasmas **5**, 1321 (1998).

[29] T. N. Carlstrom, G. L. Campbell, J. C. DeBoo, and R. Evanko *Rev. Sci Instrum.* **63**, 4801 (1992)

[30] D. M. Ponce-Marquez, B. D. Bray, T. M. Deterly, C. Liu, and D. Eldon *Rev. Sci Instrum.* **81**, 10D525 (2010)

[31] K. H. Burrell, D. H. Kaplan, P. Gohil, D. G. Nilson, R. J. Groebner, and D. M. Thomas *Rev. Sci Instrum.* **72**, 1028 (2001).

[32] C.T. Holcomb, *et al.,* Rev. Sci. Instrum. **77**, 10E506 (2006).

[33] C.Z. Cheng and M. S. Chance *Phys. Fluids* **29** 3695 (1985).

[34] Y. Kusama, H. Kimura, T. Ozeki, M. Saigusa, G.J. Kramer, T. Oikawa, S. Moriyama, M. Nemoto, T. Fujita, K. Tobita, G. Y. Fu, R. Nazikian, and C. Z. Cheng, *Nucl. Fusion* **38** 1215 (1998).

[35] Berk H L, Borba D N, Breizman B N, Pinches S D and Sharapov S E *Phys. Rev. Letters* **87** 1085002 (2001).

[36] M. A. Van Zeeland, G. J. Kramer, M. E. Austin, R. L. Boivin, W. W. Heidbrink, M. A. Makowski, G. R. McKee, R. Nazikian, W. M. Solomon, and G. Wang, Phys. Rev. Lett. **97**, 135001 (2006).

[37] M. A. Van Zeeland, W. W. Heidbrink, R. Nazikian, M. E. Austin, C. Z. Cheng, M. S. Chu, N. N. Gorelenkov, C. T. Holcomb, A. W. Hyatt, G. J. Kramer, J. Lohr, G. R. McKee, C. C. Petty, R. Prater, W. M. Solomon, and D. A. Spong, Nucl. Fusion **49**, 065003 (2009).

[38] Turnbull, A.D. et.al. *Phys. Fluids B* **5** 2548 (1993).

[39] W.W. Heidbrink, E.J. Strait, M.S. Chu and A.D. Turnbull *Phys. Rev. Letters* **71** 855 (1993).

[40] M.E. Austin and J. Lohrn *Rev. Sci. Instrum.* **74** 1457 (2003).

[41] M.A. Van Zeeland, G.J. Kramer, R. Nazikian, et.al. *Plasma Phys. Control. Fusion* **47** L31 (2005).

[42] W.W. Heidbrink, et.al. 16th IAEA Technical Meeting on Energetic Particles in Magnetic Confinement Systems-Theory of Plasma Instabilities (2019), *https://conferences.iaea.org/event/185/ contributions/14980/attachments/8173/10786/ IAEA2019_Heidbrink_invited.pdf*

[43] W.W. Heidbrink, et.al. *Nucl. Fusion* In Submission (2020)

[44] R. Nazikian, et.al. *Phys. Plasmas* **15** 056107 (2008).

[45] Heidbrink, W. W. and Taylor, P. L. and Phillips, J. A. *Rev. Sci. Instrum.* **68** 536 (1997).

[46] C. Z. Cheng and M. S. Chance, J. Comput. Phys. **71**, 124 (1987).

[47] C. Z. Cheng, Phys. Report **211**, 1 (1992).

[48] R.B. White and MS. Chance *Phys. Fluids* **27** 2455 (1984).

[49] C.S. Collins, W. W. Heidbrink, M. Podesta, et.al. *Nucl. Fusion* **57** 086005 (2017).

[50] Y. Todo, M.A. Van Zeeland, A. Bierwage and W.W. Heidbrink *Nucl. Fusion* **54** 104012 (2014).

[51] Y. Todo, M. A. Van Zeeland, A. Bierwage, W.W. Heidbrink and M.E. Austin *Nucl. Fusion* **55** 073020 (2015).

[52] Y. Todo, M. A. Van Zeeland and W.W. Heidbrink *Nucl. Fusion* **56** 112008 (2016).